CATALYSIS

Dealuminated Beta zeolite reverses Ostwald ripening for durable copper nanoparticle catalysts

Lujie Liu[1]†, Jiaye Lu[2]†, Yahui Yang[3], Wolfgang Ruettinger[3], Xinhua Gao[4], Ming Wang[5], Hao Lou[6], Zhandong Wang[6], Yifeng Liu[7], Xin Tao[8], Lina Li[8], Yong Wang[9], Hangjie Li[1], Hang Zhou[1], Chengtao Wang[1], Qingsong Luo[1], Huixin Wu[1], Kaidi Zhang[1], Jiabi Ma[5]*, Xiaoming Cao[2,10]*, Liang Wang[1]*, Feng-Shou Xiao[1,11]*

Copper nanoparticle–based catalysts have been extensively applied in industry, but the nanoparticles tend to sinter into larger ones in the chemical atmospheres, which is detrimental to catalyst performance. In this work, we used dealuminated Beta zeolite to support copper nanoparticles (Cu/Beta-deAl) and showed that these particles become smaller in methanol vapor at 200°C, decreasing from ~5.6 to ~2.4 nanometers in diameter, which is opposite to the general sintering phenomenon. A reverse ripening process was discovered, whereby migratable copper sites activated by methanol were trapped by silanol nests and the copper species in the nests acted as new nucleation sites for the formation of small nanoparticles. This feature reversed the general sintering channel, resulting in robust catalysts for dimethyl oxalate hydrogenation performed with supported copper nanoparticles for use in industry.

Metal nanoparticles (NPs) on the surface of heterogeneous catalysts encounter reactant and product molecules at high temperatures (*1*–*7*), and these conditions often cause the NPs to sinter into larger ones. The resulting loss of surface area and reduced number of active sites can lead to irreversible deactivation (*1*–*3*, *8*–*12*), and it costs billions of dollars per year to shut down the reaction process and replace the catalysts after deactivation (*13*). For metals with low melting temperatures and, hence, higher surface diffusion, such as copper, sintering can lead to deactivation for various hydrogenation (*14*, *15*) and reforming reactions (*16*, *17*).

Redispersion of the sintered metal NPs into smaller ones on the support surface could efficiently reverse deactivation. Sintering often occurs by the loss of mobile metal atoms from small NPs and diffusion and capture by larger NPs, a process known as Ostwald ripening (*18*–*20*). Reversing this process would require activation of the metal sites on large NPs and the capture of these metal species by the support. However, this process requires hybrid supports that have distinguishable interactions with the metal species that cause them to move from a weak-interaction region to a strong-interaction region (*9*, *21*). For example, Cu species migrated from silica to the ceria on the SiO_2-CeO_2 mixed supports to form smaller clusters (*21*), but this movement changed the intrinsic catalytic properties of the Cu NPs.

The reverse ripening of metal NPs on a homogeneous support should return the sintered catalysts to ones with identical performances to the original catalysts, but achieving this is thermodynamically challenging. Treatment with halogens that coordinate with the metal sites can initiate their emission from bulky NPs and transmission on the support. Such postregeneration of the deactivated catalysts (*22*–*24*) has been used in industrial processes, such as oxychlorination for redispersing Pt NPs on alumina support (*23*), which can generate environmentally unfriendly wastes and corrode the reactor. Ideally, in addition to the postregeneration of deactivated catalysts, the redispersion that occurs under the reaction processes would realize a catalyst with superior durability against sintering (*25*–*27*).

We report that dealuminated Beta zeolite (Beta-deAl, Si/Al atomic ratio at ~1250; fig. S1) is an efficient support for the reverse ripening of Cu NPs in methanol vapor at 200°C. This feature maintained small Cu NPs (2 to 3 nm) and even redispersed large Cu particles (15 to 250 nm) on siliceous Beta-deAl support. We focused on dimethyl oxalate (DMO) hydrogenation, a structure-dependent reaction that has been industrially used for the conversion of coal to ethylene glycol (EG) (*28*, *29*). As a result, the Cu/Beta-deAl catalyst maintains high conversion and selectivity in a continuous reaction for long periods, even during ambient-pressure DMO hydrogenation.

Redispersion of Cu NPs

We performed a proof-of-concept experiment by comparing the stability of Beta-deAl (Cu/Beta-deAl; figs. S1 and S2) and amorphous silica–supported Cu NPs (Cu/SiO_2, Cu loading content at 3.0 wt %) in methanol vapor. The Cu NP sizes and distributions were initially characterized by scanning transmission electron microscopy (STEM). The fresh Cu/SiO_2 (as prepared by calcination in air and prereduction in hydrogen) showed that the NPs had an average size of 3.0 ± 0.8 nm (fig. S3, A and D). After the methanol treatment at 200°C for 12 hours (methanol feeding rate of 0.03 ml_{liquid} min^{-1} in hydrogen with a flow rate of 15 ml min^{-1}), the Cu NPs on Cu/SiO_2 sintered into ones with an average size of 4.0 ± 1.4 nm (fig. S3, B and E), and some NPs were larger than 7.0 nm (fig. S3, C and E). Methanol-triggered Cu sintering is known to occur under similar conditions and leads to the deactivation of Cu catalysts in industrial processes (*7*, *28*–*30*). However, the Cu NPs on the Cu/Beta-deAl (Cu content at 3.0 wt %) exhibited an opposite phenomenon after the equivalent methanol treatment. The initial average Cu NP size of 5.6 ± 1.6 nm (fresh catalyst; Fig. 1A and fig. S4, A and B) was reduced to 2.4 ± 0.7 nm, and we could not detect NPs larger than 6.5 nm (Fig. 1B and fig. S4, C and D). The Cu content (3.0 wt %) was unchanged after the methanol treatment. These results suggest a redispersion of Cu NPs on the Cu/Beta-deAl in methanol vapor.

The redispersion of Cu NPs on Cu/Beta-deAl was further confirmed by in situ x-ray diffraction (XRD) characterization. Compared with the bare Beta-deAl zeolite, the fresh Cu/Beta-deAl exhibited peaks at 43.3° and 36.5° that we assigned to metallic Cu and Cu_2O phases, respectively (*31*, *32*) (Fig. 1C and fig. S5). Methanol treatment reduced these diffraction peaks until they disappeared after 12 hours, which confirmed the elimination of large Cu or Cu_2O particles. These results were consistent with those of the TEM characterizations and supported the reversed Cu sintering on the Cu/Beta-deAl in methanol vapor (Fig. 1D). By contrast, after the equivalent methanol vapor treatment, the diffractions of Cu-related NPs were enhanced on the Cu/SiO_2 because of the formation of larger Cu NPs (fig. S6). These results suggest that the Beta-deAl zeolite was crucial for the redispersion of Cu. The Cu NPs on other zeolites,

[1]Key Lab of Biomass Chemical Engineering of Ministry of Education, College of Chemical and Biological Engineering, Zhejiang University, Hangzhou 310027, China. [2]Joint International Research Laboratory of Precision Chemistry and Molecular Engineering, Feringa Nobel Prize Scientist Joint Research Center, School of Chemistry and Molecular Engineering, East China University of Science and Technology, Shanghai 200237, China. [3]BASF Advanced Chemicals Co., Ltd., Shanghai 200137, China. [4]State Key Laboratory of High-efficiency Utilization of Coal and Green Chemical Engineering, School of Chemistry and Chemical Engineering, Ningxia University, Yinchuan 750021, China. [5]Key Laboratory of Cluster Science of Ministry of Education, School of Chemistry and Chemical Engineering, Beijing Institute of Technology, Beijing 102488, China. [6]National Synchrotron Radiation Laboratory, University of Science and Technology of China, Hefei, Anhui 230029, China. [7]Department of Chemistry, Zhejiang University, Hangzhou 310027, China. [8]Shanghai Institute of Applied Physics, Chinese Academy of Sciences, Shanghai 201204, China. [9]Center of Electron Microscopy and State Key Laboratory of Silicon Materials, School of Materials Science and Engineering, Zhejiang University, Hangzhou 310027, China. [10]School of Chemistry and Chemical Engineering, Shanghai Jiao Tong University, Shanghai 200240, China. [11]Beijing Advanced Innovation Center for Soft Matter Science and Engineering, Beijing University of Chemical Technology, Beijing 100029, China.
*Corresponding author. Email: majiabi@bit.edu.cn (J.M.); xmcao@ecust.edu.cn (X.C.); liangwang@zju.edu.cn (L.W.); fsxiao@zju.edu.cn (F.-S.X.)
†These authors contributed equally to this work.

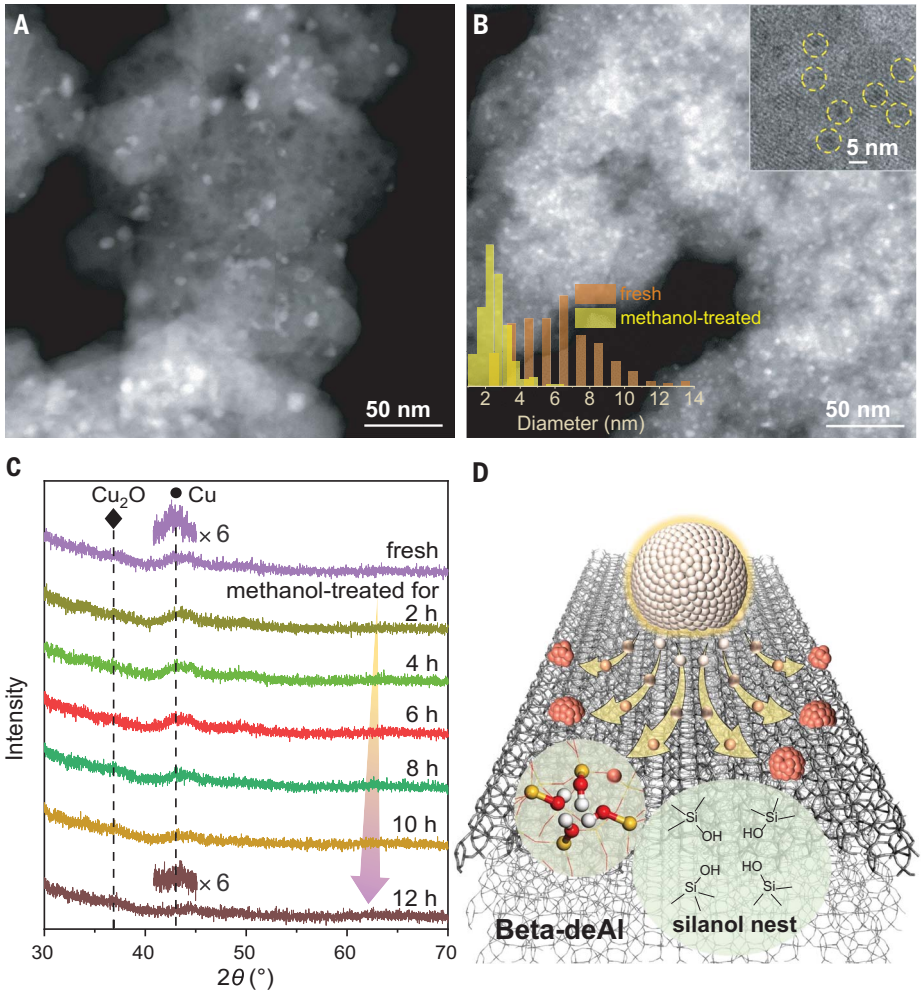

Fig. 1. Redispersion of Cu on the Beta-deAl support by methanol treatment. (**A** and **B**) High-angle annular dark-field STEM images of fresh Cu/Beta-deAl (A) and Cu/Beta-deAl (B) after the methanol treatment at 200°C for 12 hours. The insets in (B) show Cu NP size distributions of the fresh and methanol-treated catalysts (bottom left) and a high-resolution TEM image of the methanol-treated catalyst (top right). (**C**) In situ XRD patterns characterizing the change of Cu NPs on the Cu/Beta-deAl during the methanol treatment at 200°C. (**D**) Illustration showing the reverse Ostwald ripening of Cu NPs on the Beta-deAl support. The silanol nest, which is formed after removing the tetracoordinated Al sites from the Beta zeolite framework, usually involves four silanols in a local region with hydrogen bonds between them.

such as commercial Beta (Si/Al ratio at 13), ZSM-5 (aluminosilicate MFI zeolite with Si/Al ratio at 13), S-1 (siliceous MFI zeolite), and silanol-modified MFI zeolites (ZSM-5-OH and S-1-OH), also readily sintered into larger NPs after the methanol treatment at 200°C (figs. S7 to S12).

Catalytic evaluation

We evaluated Cu/SiO_2 and Cu/Beta-deAl in the hydrogenation of DMO in methanol vapor at 200°C with a liquid hourly space velocity (LHSV) of 0.8 $hour^{-1}$ (ml_{DMO} ml_{cat}^{-1} $hour^{-1}$) based on a feeding rate of DMO per milliliter of catalyst. The data that characterize the performances are shown in Fig. 2A, where the initial DMO conversions were maintained at ~40% for evaluating the catalyst durability. The Cu/SiO_2 catalyst showed continuously decreased DMO conversion with reaction time; the conversion of 35.2% after 24 hours dropped to 19.8% after 80 hours and to 9.1% after 110 hours. TEM characterization of the spent Cu/SiO_2 catalyst after testing for 80 hours showed an average Cu NP size of 4.4 ± 1.3 nm (fig. S13), which was larger than that of the fresh catalyst (3.0 ± 0.8 nm). In previous studies of DMO hydrogenation, abundant methanol in the reaction system, from the solvent and product, also caused Cu sintering (*28*–*31*).

In the DMO hydrogenation under equivalent conditions for Cu/Beta-deAl, we observed improved DMO conversion over time; conversion increased from 33.4 to 45.0% in the initial 12 hours and then remained at 45.1 to 48.1% in the test for another 188 hours (Fig. 2A). TEM characterizations of the spent Cu/Beta-deAl after reaction for 10 hours showed an average Cu NP size of 2.3 ± 0.4 nm (fig. S14) versus 5.6 ± 1.6 nm for the fresh sample. This result confirmed a self-optimization process in the initial reaction. Interestingly, the formed small-size Cu NPs on the Cu/Beta-deAl were constant during the reaction period, and the average Cu NP size was 2.5 ± 0.7 nm on the spent Cu/Beta-deAl after testing for 80 hours (fig. S15). In the reaction with 1,4-dioxane as solvent, the Cu/Beta-deAl catalyst also exhibited constant performance, with an average Cu NP size of 2.4 ± 0.9 nm after reaction for 120 hours (figs. S16 and S17).

We then adjusted the LHSV of DMO for evaluating the catalysts with high or even full conversion of DMO. After pretreatment with methanol vapor at 200°C for 10 hours, the Cu/Beta-deAl exhibited full DMO conversion under given reaction conditions (LHSV at 0.4 $hour^{-1}$, 200°C) with EG selectivity >98.5% (Fig. 2B). Increasing the LHSV to 0.8 $hour^{-1}$ resulted in a lower DMO conversion at 45.4% with methyl glycolate (MG) from semihydrogenation as a dominant product. This incomplete conversion provided a way to evaluate the activity change of the Cu catalysts. In a continuous test for 120 hours, we periodically switched the LHSV between 0.4 and 0.8 $hour^{-1}$ every 30 hours, and the Cu/Beta-deAl exhibited constant performance in each period. For example, after the test in which the LHSV was at 0.8 $hour^{-1}$ and was then switched back to 0.4 $hour^{-1}$, the Cu/Beta-deAl catalyst gave a DMO conversion and EG selectivity similar to those in the initial reaction. By contrast, the Cu/SiO_2 showed continuously decreased DMO conversion with reaction time, suggesting a deactivation process (Fig. 2B).

The durability of Cu/Beta-deAl was further evaluated under a constant condition (LHSV at 0.4 $hour^{-1}$, 200°C) for 200 hours. After an activation period of 12 hours, the DMO was fully converted, with EG selectivity up to 98.7% (Fig. 2C). In this case, the selectivity to ethanol and other heavier products was <0.5%. A longer reaction life was reasonably expected because of the undetectable deactivation trend and unchanged Cu NP size (average size of 2.7 ± 0.7 nm; figs. S18 and S19) after the test. However, the Cu NPs on the other zeolites, such as S-1, ZSM-5, and aluminosilicate Beta zeolites, exhibited EG yields that were much lower than that of the Cu/Beta-deAl (fig. S20).

A high EG selectivity under full conversion of DMO at sufficient LHSV is required for potential commercial utilization. By raising the Cu loading content to 18 wt % on Beta-deAl support, DMO hydrogenation was efficiently catalyzed under a rapid feed. For example, at 200°C with a LHSV of 1.8 $hour^{-1}$, an EG yield of ~96.2% at full DMO conversion was obtained without any deactivation trend in the

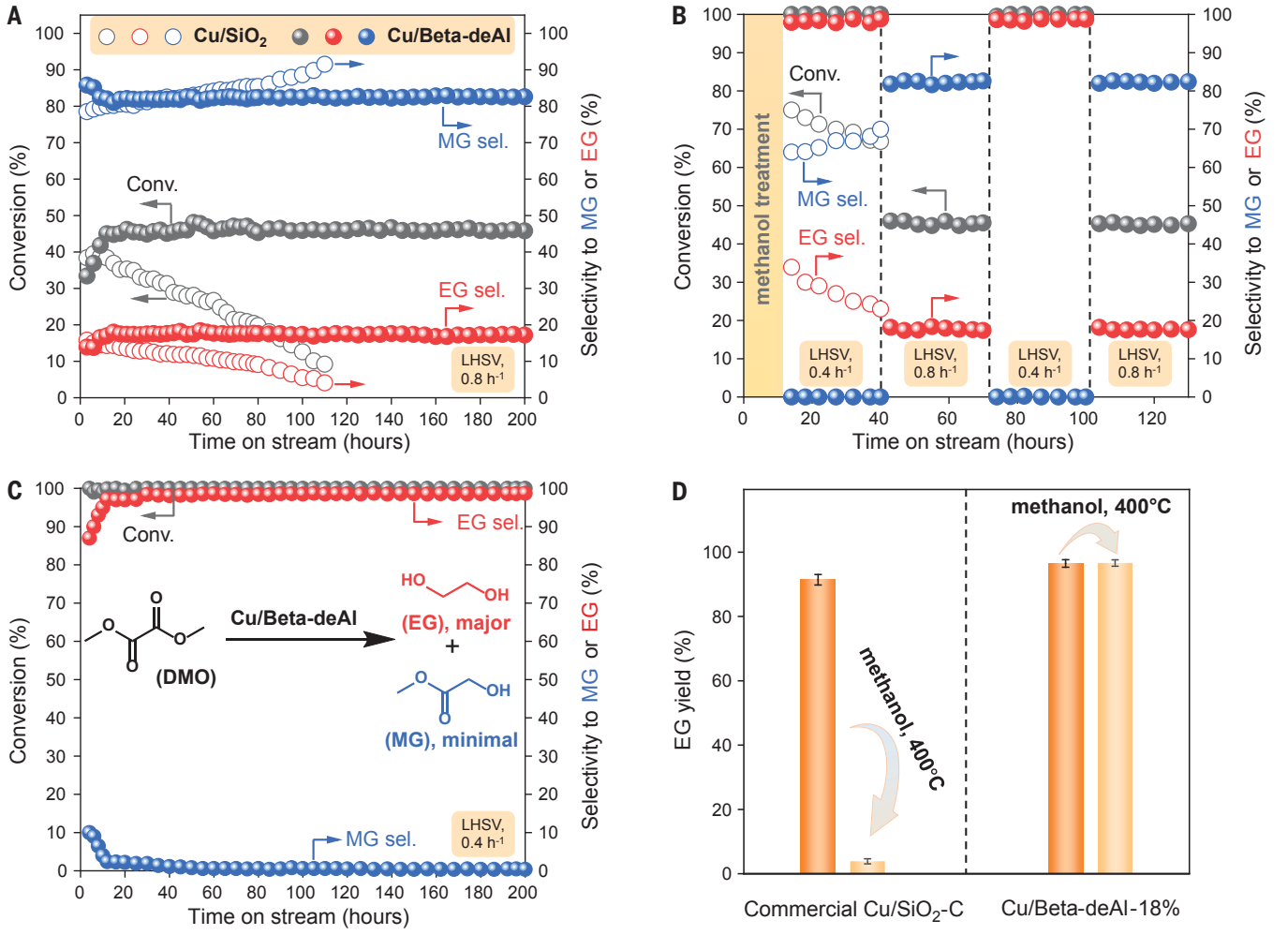

Fig. 2. Catalytic tests in DMO hydrogenation. (**A**) Catalytic performances of the Cu/SiO_2 (open circles) and Cu/Beta-deAl (solid circles) in DMO hydrogenation. Reaction conditions were as follows: 200°C, 2.5 MPa, LHSV of 0.8 $hour^{-1}$, and $n(H_2)/n(DMO)$ of 45. (**B**) Effect of the methanol treatment (initial 10 hours) on the performances of the Cu/SiO_2 and Cu/Beta-deAl catalysts in DMO hydrogenation. (**C**) Data showing the durability of the Cu/Beta-deAl catalyst in DMO hydrogenation. Reaction conditions were as follows: 200°C, 2.5 MPa, and LHSV of 0.4 $hour^{-1}$. (**D**) Data showing the EG yields in DMO hydrogenation over fresh and methanol-treated commercial Cu/SiO_2-C and Cu/Beta-deAl-18% catalysts. Conditions for methanol treatment were as follows: methanol feeding rate of 0.03 ml_{liquid} min^{-1}, 400°C, and 48 hours. The error bars represent standard deviation.

test for 200 hours (fig. S21). By contrast, the commercial silica-supported Cu-based catalyst (Cu/SiO_2-C) under the same conditions showed an EG yield at 90.1 to 93.4% (table S1). Even after raising the LHSV as high as 3.0 $hour^{-1}$, the Cu/Beta-deAl-18% still catalyzed the full DMO conversion with an EG selectivity at 95.8% (table S2).

The DMO hydrogenation is exothermic, so inadequate heat transfer could form hot regions in the industrial reactor that cause irreversible catalyst deactivation from Cu sintering (*33*). To evaluate thermal stability under harsh conditions, the Cu/Beta-deAl-18% and commercial Cu/SiO_2-C were treated in methanol vapor at 400°C for 48 hours and then tested in the DMO hydrogenation. As shown in Fig. 2D, the EG yields over the Cu/Beta-deAl-18% (full DMO conversion with EG selectivity at 96.5%) were unchanged before and after the treatment, whereas the Cu/SiO_2-C was obviously deactivated, given the extremely low EG yield at 3.9% (DMO conversion at 45.4%, EG selectivity at 8.6%). Characterizations by XRD and TEM showed that the sintered Cu NPs had an average diameter of up to 7.4 ± 3.3 nm on the Cu/SiO_2-C after the methanol treatment at 400°C (fig. S22), whereas the Cu/Beta-deAl-18% exhibited Cu NPs with an average size of 3.8 ± 1.0 nm and even had abundant ones that were smaller than 3.0 nm (fig. S23).

The DMO hydrogenation at ambient pressure poses greater challenges to catalyst stability. A previous study achieved efficient DMO hydrogenation at ambient pressure on a Cu/SiO_2 catalyst with fullerene as an electron buffer, but the Cu sintering still occurred, as suggested by the XRD characterization (*28*). The Cu/SiO_2 catalyst without an electron buffer deactivated quickly during the ambient-pressure reaction (*28*, *34*–*36*). Interestingly, the Cu/Beta-deAl-18% could efficiently catalyze the DMO hydrogenation, resulting in an EG yield of 90.8% at 200°C under an LHSV of 0.6 $hour^{-1}$ and an EG yield of 90.1% at 230°C at an LHSV of 3.6 $hour^{-1}$; both reactions were performed at ambient pressure (fig. S24 and table S3). This catalyst was stable in the continuous reaction for 300 hours and maintained a Cu NP size of 4.0 ± 1.0 nm (figs. S24 and S25). In addition to the Cu sintering, another issue that challenges the durability of general $Cu-SiO_2$–based catalysts is silica leaching, in which the tetramethoxysilane-related species is formed in methanol vapor and leached from the catalyst (*37*, *38*). By contrast, this problem was efficiently avoided on the Cu/Beta-deAl catalyst (fig. S26) because of the superior stability of crystallized zeolite in methanol vapor (*39*–*41*) relative to the amorphous silica.

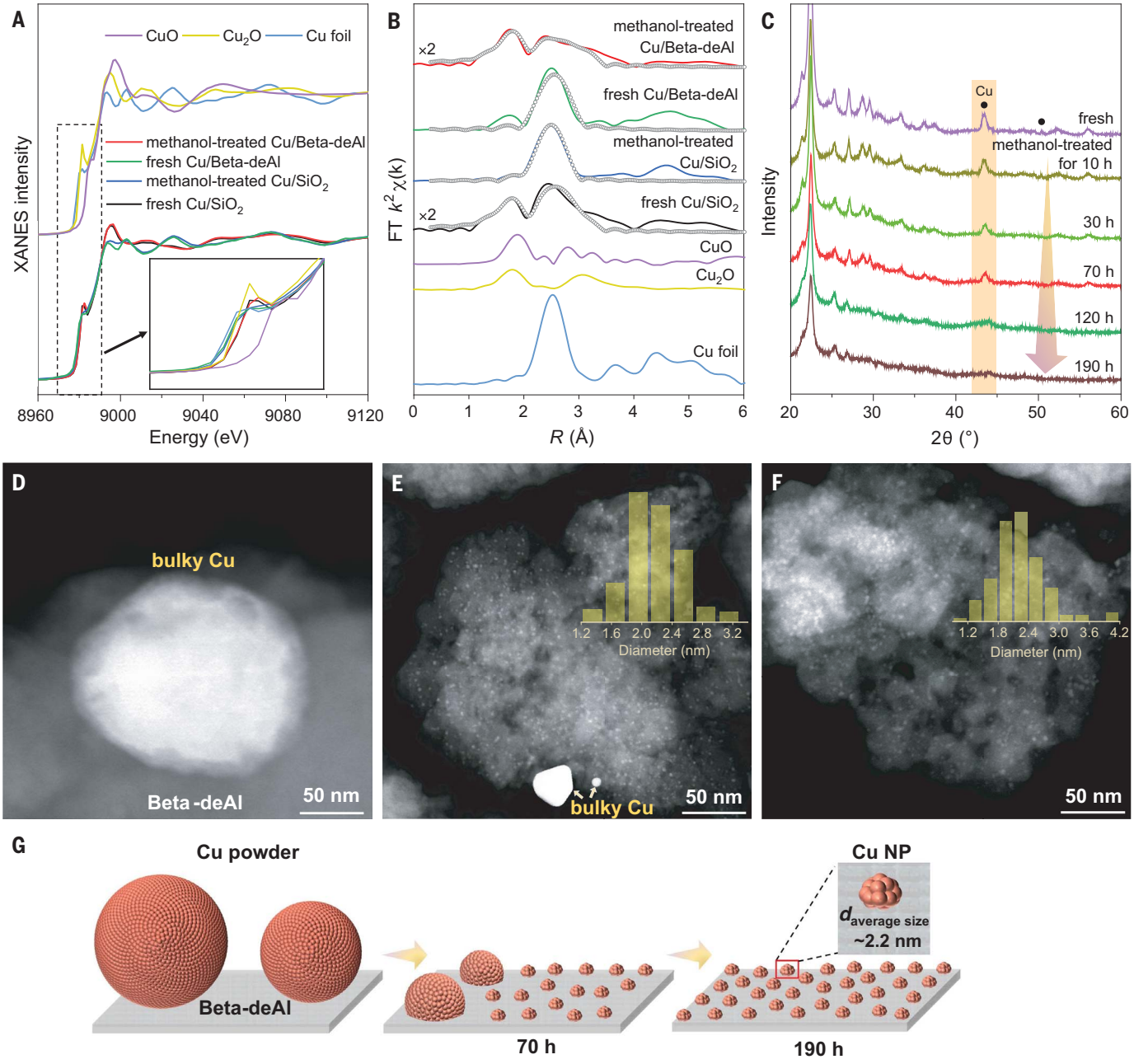

Fig. 3. Methanol-triggered structure change of the Cu particles. (**A**) Normalized Cu *K*-edge XANES spectra of fresh and methanol-treated Cu/SiO_2 and Cu/Beta-deAl catalysts. The methanol treatments were performed at 300°C for 12 hours. (**B**) Fourier-transformed (FT) magnitudes of the experimental Cu *K*-edge EXAFS spectra. The plot lines with open circles show fitting results of samples. *R*, bond distance. (**C** to **F**) XRD patterns (C) and STEM images [(D) to (F)] characterizing the mixture of Cu powder and Beta-deAl zeolite during the methanol treatment at 200°C for different periods. The insets in (E) and (F) show particle size distribution of small Cu NPs. (**G**) Illustration showing the formation of small-size Cu NPs on the Beta-deAl zeolite from the physically mixed commercial Cu powder. *d*, diameter.

Characterizations

In situ XRD characterizations of the Cu/Beta-deAl in methanol vapor at different temperatures showed that the redispersion of Cu NPs was undetected at 100°C (fig. S27A) but detected at 200°C (fig. S5) and accelerated at 300°C (fig. S27B). Further raising the treatment temperature to 400°C resulted in Cu NPs of similar size to those obtained with the fresh Cu/Beta-deAl catalyst (figs. S27C and S28). These results suggest that the redispersion of the Cu NPs was related to the temperature. The influence of methanol partial pressure was investigated at 200°C, where the higher methanol partial pressure (e.g., >67 kPa) would benefit the Cu redispersion (fig. S29). A general view on the methanol-triggered Cu sintering includes methanol decomposition to form CO and CO-initiated Cu migration (*30*, *34*, *42*). However, CO was unable to change the average diameter of Cu NPs by exposure of Cu/Beta-deAl to a CO atmosphere at 200°C (figs. S30 and S31). The other molecules, such as H_2, N_2, and water, were also unable to decrease the Cu NP sizes (figs. S30 and S31). Formaldehyde, which was produced from the methanol dehydrogenation (fig. S32), greatly promoted the redispersion of Cu particles, resulting in an average Cu NP size of 2.3 ± 0.9 nm for the formaldehyde-treated Cu/Beta-deAl sample (figs. S30 and S33).

We characterized the Cu/SiO_2 and Cu/Beta-deAl catalysts before and after the methanol treatment at 300°C (the temperature required to amplify sintering or redispersing NPs on the catalysts) by x-ray absorption fine structure spectroscopy. The x-ray absorption near-edge structure (XANES) spectrum of fresh Cu/SiO_2 fell between those of Cu foil and Cu_2O, which suggested a multivalent Cu^0 and Cu^+ composition (Fig. 3A) that was consistent with the general feature of the Cu/SiO_2 with $Cu^{\delta+}$-O-SiO_x interaction (*7*, *28*–*31*, *34*, *43*). The methanol-treated Cu/SiO_2 was more metallic because the spectrum was near that of the Cu foil that was caused by Cu NPs sintering that destroyed the interaction with silica. Extended x-ray absorption fine structure (EXAFS) analysis (Fig. 3B) showed an increased coordination number (CN) of the Cu-Cu shell (3.5 to 8.2) and the absence of Cu-O or Cu-O-Cu signals after the methanol treatment (table S4).

By contrast, the fresh Cu/Beta-deAl exhibited a XANES spectrum near that of Cu foil. After the methanol treatment, the Cu species were partially oxidized, giving a XANES spectrum near that of Cu_2O. The EXAFS fitting results showed the CN of the Cu-Cu shell at 9.0 on the fresh Cu/Beta-deAl, which dropped to 2.3 with the CN of the Cu-O shell at 1.5 and the CN of the Cu-O-Cu shell at 1.7 on the methanol-treated sample (Fig. 3B and table S4). Considering that the methanol treatment with hydrogen carrier provided a reductive environment, the formation of more-oxidized Cu species could be attributed to the formation of a $Cu^{\delta+}$-O-SiO_x interaction during the methanol-triggered redispersion of Cu.

Redispersion of bulky Cu particles

The redispersion of Cu on the Beta-deAl zeolite was further confirmed by methanol treatment of a physical mixture containing Beta-deAl and commercial Cu powders (15 to 250 nm; figs. S34 and S35). The XRD patterns recorded the change of Cu crystals in methanol vapor for different periods. The diffraction peaks assigned to Cu crystals decreased in intensity during the treatment period, which suggested a continuous migration of Cu species from the bulky crystals (Fig. 3C). A STEM image of the fresh sample showed only bulky Cu particles with undetectable small Cu NPs (Fig. 3D). The small-size Cu NPs were observed on the Beta-deAl support when methanol was introduced to the mixture at 200°C (an initial stage of 5 hours; fig. S36). After the methanol treatment at 200°C for 70 hours, more Cu NPs appeared with an average particle size of 2.1 ± 0.4 nm (Fig. 3E and fig. S37; bulky ones were not included in the calculation), whereas the bulky Cu particles were still observed but their sizes were smaller than those of the parents. After the treatment in methanol vapor for 190 hours, the Cu peaks were undetectable in the XRD pattern, which confirmed the removal of bulky Cu crystals. A STEM image of the sample showed an average Cu NP size of 2.2 ± 0.5 nm on the Beta-deAl support, with undetectable bulky Cu particles (Fig. 3F and figs. S37 and S38). The equivalent test on the mixture of commercial Cu powders with amorphous silica resulted in unchanged XRD patterns, and small Cu NPs were absent (figs. S39 and S40). Based on these results, we present a schematic illustration showing the formation of small-size Cu NPs on the Beta-deAl zeolite from the bulky Cu crystals (Fig. 3G).

Mechanism study

Previous studies have shown that the Cu on relatively inert supports such as silica sinters through particle migration and coalescence under thermal conditions but tends to proceed by Ostwald ripening under chemical triggering conditions (*8*, *20*, *43*), such as the hydrogenation in methanol vapor. The ripening route involves the formation and diffusion of metal atoms, complex intermediates, or both (*20*, *44*, *45*). A support with strong interactions might trap the metal atoms or complex intermediates. We used synchrotron vacuum ultraviolet photoionization mass spectrometry (SVUV-PIMS; fig. S41) to detect Cu species in methanol vapor. In these tests, methanol was introduced to the physical mixture of Cu powder with Beta-deAl, and the possible intermediates were captured through a vacuum channel and detected by mass spectrometry. The signals of methoxyl [mass/charge ratio (m/z) of 31] and formaldehyde (m/z of 30) species from methanol conversion (m/z of 32) appeared (Fig. 4A), as well as other possible species of $(CHO)Cu_1$* (m/z of ~92 and 94), $(CH_2O)Cu_1$* (m/z of ~93 and 95), and $(CH_3O)Cu_1$* (m/z of ~94 and 96) (Fig. 4B). These results suggest the existence of Cu_1-related intermediates during the migration. In addition, the signal intensities for $(CHO)Cu_1$* and $(CH_3O)Cu_1$* gradually increased with temperature during the methanol treatment (fig. S42), which is related to the easier formation and faster escape of these intermediates at higher temperatures. These insights are in good agreement with general knowledge about the Ostwald ripening processes with chemical-triggered metal sintering (*8*, *20*, *44*–*47*), but here we provide direct experimental evidence and also reverse this process with the Beta-deAl support.

We also performed density functional theory (DFT) calculations, in which we first considered the desorption of a Cu atom from the Cu NP matrix as the primary step that initiates ripening. The direct detachment of a Cu atom from the matrix is difficult because of the strong Cu–Cu bonding, but the methanol-derived species could coordinate with the surface Cu atom and induce its migration. We considered the formation process of methanol-derived species (Fig. 4C and figs. S43 and S44) and showed that the production of $*CH_3O$, *CHO, and *CO was exothermic, whereas the production of other species was endothermic (figs. S43 and S44 and table S5). Lower energy inputs for the Cu detachment and migration than for the ligand desorption for $(CHO)Cu_1$* and $(CH_3O)Cu_1$* suggest that the migration is more favorable in the reverse ripening process (fig. S43). For example, the *CHO exhibited an energy input of 0.42 eV for Cu detachment and migration from the Cu matrix to the silanol nest (four silanols in a local region; fig. S45), whereas direct desorption of the *CHO without Cu detachment required 1.03 eV (fig. S43). These results indicated that the complexes would preferentially detach the Cu atoms from the surface of the Cu matrix to form the intermediates that were ready for the migration, which is consistent with the results of SVUV-PIMS. In this case, lower energy inputs for $(CHO)Cu_1$* migration from the Cu matrix to the silanol nest than for $(CH_3O)Cu_1$* suggest that $(CHO)Cu_1$* is a preferential intermediate in the reverse ripening process.

The *CHO could be further dehydrogenated into *CO, but the *CO was unable to assist with the detachment of Cu atoms from the Cu matrix; thus, CO would be directly desorbed at the reaction temperature (fig. S43), which is in good agreement with the experimental results (fig. S30). In addition, the free-energy barrier for the dehydrogenation of *CHO to *CO was slightly lower than that of $(CHO)Cu_1$* moving from the matrix to the Cu/Beta-deAl surface (0.29 eV). These results indicated that *CHO decomposition to CO competes with the detachment of $(CHO)Cu_1$* (fig. S44).

We further studied the methanol-triggered Cu detachment by exploring the reactions between the gas-phase Cu_x^+ clusters and methanol with time-of-flight mass spectrometry (*48*, *49*). In our tests, the $^{63}Cu_2^+$ cations were generated by laser ablation of the Cu matrix surface, and then methanol was introduced for reaction. As shown in Fig. 4D, the peak intensity of $^{63}Cu_2^+$ decreased after reaction with methanol and led to the formation of abundant Cu_1 species [$^{63}Cu_1(CH_3OH)^+$]. Increasing the partial pressure of methanol further reduced the Cu_2^+ and enhanced the Cu_1^+ signal magnitudes. Although the reactions of $^{63}Cu_2^+$ with CH_3OH could not fully represent the types of ligand-Cu intermediate because of the obvious scale difference between the atomic $^{63}Cu_2^+$ cluster and Cu NP surface, these results strongly supported that methanol triggers Cu–Cu bond cleavage. In sharp contrast, the $^{63}Cu_2^+$ cations were inert toward CO and H_2 under similar reaction conditions, which confirms the undetectable ability of these gases to trigger the Cu detachment (Fig. 4D). These results were also in good agreement with the results obtained when Cu/Beta-deAl catalyst was treated with CO and H_2 (figs. S30 and S31).

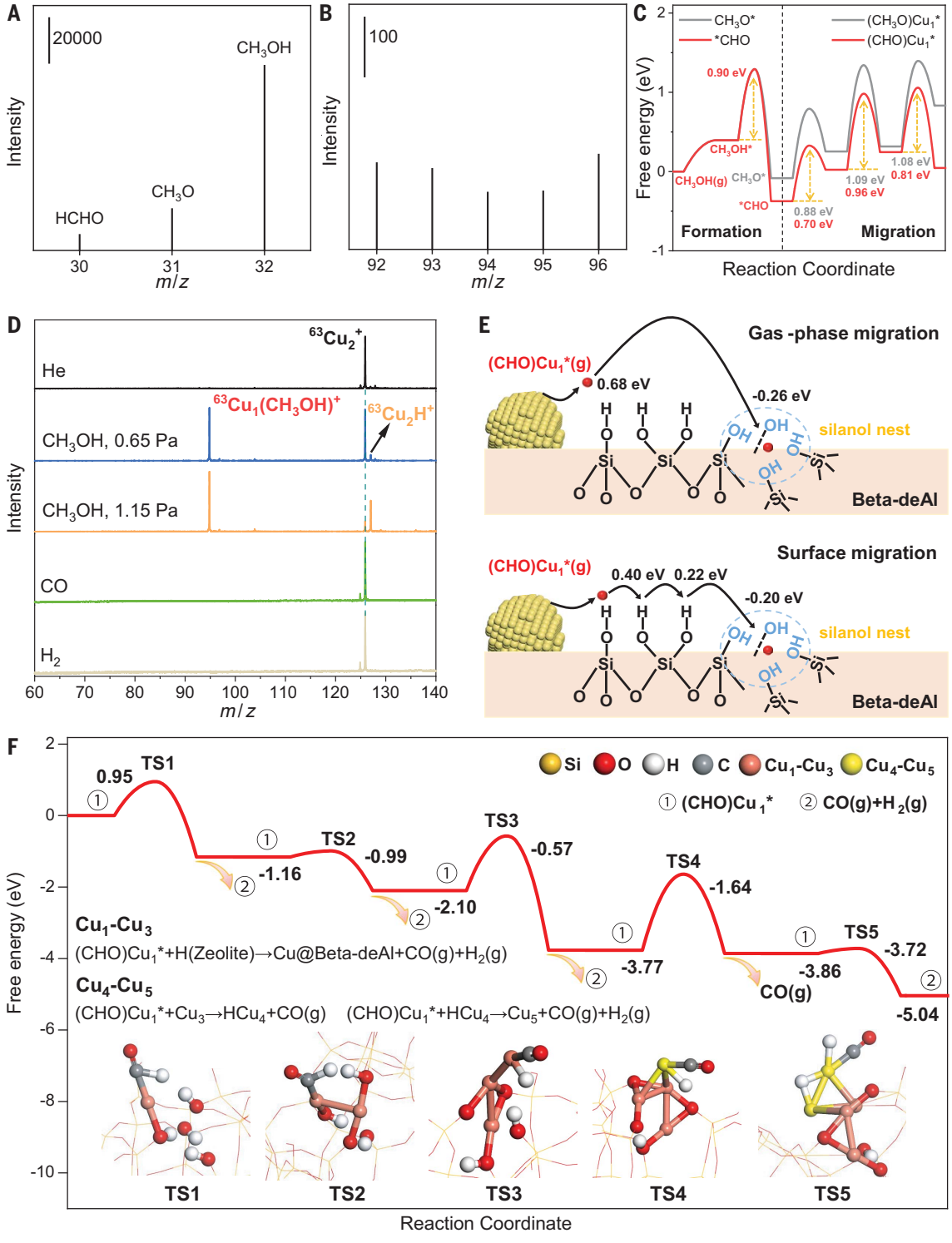

Fig. 4. Experimental and theoretical insights of the reverse ripening process. (**A** and **B**) Data showing the signals at different *m/z* regions in the SVUV-PIMS tests that characterize the mixture of Cu powder and Beta-deAl during methanol treatment. The background signals were excluded. The possible species corresponding to the peaks are given, where the signal of *m/z* 31 should be from the fragmentation of methanol. (**C**) Free energies of $(CH_3O)Cu_1$* and $(CHO)Cu_1$* intermediates, and the formation and migration of the Cu_1 intermediates from the Cu particles to surface hydroxy groups with the methanol treatment. (**D**) Time-of-flight mass spectra for reactions of the mass-selected $^{63}Cu_2^+$ cations with methanol, CO, and hydrogen. The reaction time was about 1.1 to 1.2 ms, and the effective reactant gas pressures for CO and H_2 were around 1.0 Pa. (**E**) Illustration showing the gas-phase and surface migration of Cu species on the catalyst surface. (**F**) Energy profile showing the nucleation process from Cu_1 to Cu_5 at the silanol nests. TS, transition state; Cu_x, Cu cluster with *x* number of Cu atoms.

With respect to the migration of Cu_1 intermediates on the zeolite surface, both surface and gas-phase migration might occur during the reverse Ostwald ripening process (figs. S46 to S49) (*20*, *25*, *27*, *34*, *44*–*46*). With the $(CHO)Cu_1$ intermediate as a model, the gas-phase migration would cost 0.68 eV for desorption from the solid surface and −0.26 eV for capture by the silanol nests (Fig. 4E). In the case of surface migration (Fig. 4E), the first step is the migration of the $(CHO)Cu_1$ intermediate from the Cu cluster to the adjacent terminal silanol on the zeolite surface (0.40 eV). Next, the $(CHO)Cu_1$* migrates on the terminal silanol (0.22 eV) (*20*) and finally arrives at the silanol nest (−0.20 eV). Slightly lower energy input indicates that the surface migration would be the preferential pathway for $(CHO)Cu_1$* diffusion during the dynamic change of the Cu species that occurs with the methanol treatment.

Figure 4F shows an energy diagram that characterizes the stepwise nucleation process by which the silanol nest captures the $(CHO)Cu_1$* intermediate, which, with a free energy of −1.16 eV, is obviously exothermic. With respect to the interaction between $(CHO)Cu_1$* and the silanols in the nest, a stable $Cu^{\delta+}$-$(OSi)_2$ linkage

with adjacent silanol groups formed, which was supported by a crystal orbital Hamilton population (COHP) analysis (figs. S50 and S51). CO and H_2 were preferentially produced from the reaction between *CHO and the hydrogen of the silanols (fig. S52). As a result, the Cu_1 intermediates could be captured, and the silanol nest of the Beta-deAl zeolite displayed a crucial role because of its strong interaction with the Cu sites (fig. S53). This result is further supported by Fourier transform infrared spectroscopy, which showed the reduced signals that were associated with silanol nests on the Cu/Beta-deAl during the methanol treatment (fig. S54). However, the Beta zeolites with a different dealumination degree (table S6) and the different MFI zeolites, which both have a relatively low content of silanol nests, failed to realize the Cu redispersion (figs. S11, S12, and S55 to S59).

Compared with the silanol nest, the terminal silanol has a much weaker interaction with the $(CHO)Cu_1$* intermediate, as confirmed by the COHP values that represent the strength of the Cu–O bond (fig. S50). This renders the terminal silanols inoperable with respect to capturing the Cu intermediate (fig. S52), where these $(CHO)Cu_1$* intermediates would be trapped by another bulky Cu particle, leading to Ostwald ripening (*20*, *43*). As a result, the general Cu/SiO_2 catalyst with only terminal silanols failed to have a redispersing feature but caused the rapid Cu sintering to form larger particles (*29*, *33*, *34*, *36*, *43*). To further confirm this hypothesis, we rationally synthesized a siliceous Beta zeolite (Beta-Si) with abundant terminal silanols rather than silanol nests (fig. S58) and used it as support for Cu NPs. Cu sintered rather than redispersed after the methanol treatment on the Beta-Si (fig. S60).

After capturing the first Cu atom, the silanol nest with a Cu atom became a nucleation site, and the second and third $(CHO)Cu_1$* species were captured under the assistance of silanol groups to form Cu_3 clusters with a total free-energy change less than −2.61 eV. The Cu clusters were efficiently stabilized by the $Cu^{\delta+}$-OSi linkage, which was in good agreement with the experimental results on abundant positively charged Cu sites after the methanol treatment (Fig. 3, A and B). The Cu_3 cluster could efficiently capture more Cu_1-CHO intermediates, with a total free-energy change at −1.27 eV for capturing the fourth and fifth Cu atoms, which finally led to the formation of small-size Cu NPs (Fig. 4F). Regarding the single step of Cu_1 intermediate capture on the Cu_4 cluster to form a Cu_5 cluster at the silanol nests, the adsorption energy is −2.80 eV, whereas the Cu_1 adsorption on the bulky Cu surface is −2.22 eV (table S7). These results suggest that it is more energetically favorable for Cu_1 to be trapped by the small Cu clusters at the silanol nest than at the bulky Cu surface. We also considered the channel of Cu migration from the Cu_5 cluster at the silanol nests, through $(CHO)Cu_1$* intermediates to bulky Cu particles with the formation of CO and H_2, which is known as the classical Ostwald ripening route. This process is endothermic, with an energy of 0.76 eV. These findings indicate that the nucleation of Cu atoms at locations with small Cu clusters at silanol nests is preferred over ripening on larger Cu particles.

The redispersion of Cu NPs on the Cu/Beta-deAl thus appeared to proceed through the following steps: (i) the activation of an alcohol molecule on the surface of the Cu matrix to promote the cleavage of the Cu–Cu bond, (ii) the formation of the Cu_1 intermediate, (iii) the migration of the Cu_1 intermediate to silanol nests, and (iv) the anchoring of the Cu_1 and then more Cu atoms to form clusters. The silanol nest capture and methanol decomposition would cooperatively regulate the $(CHO)Cu_1$-mediated reverse ripening route. Notably, except for methanol, the other alcohols such as ethanol, *n*-propanol, *n*-butanol, and *n*-pentanol failed to trigger the redispersion of Cu under the equivalent tests (fig. S61). We calculated the free energy in each step for the Cu NP redispersion process for different alcohols. As shown in table S8, the biggest difference in the energy diagram for the alcohol-triggered Cu redispersion occurred at the step during which the $(RCO)Cu_1$* intermediate was captured by the silanol nests. The results show that the migration of $(RCO)Cu_1$* intermediates with butanol to the silanol nests is much more difficult than with methanol. The $(RCO)Cu_1$* with a longer carbon chain would have a larger steric hindrance (fig. S62), thus prohibiting the redispersion of Cu species on Beta-deAl.

Discussion

We have demonstrated the reverse ripening phenomenon of Cu NPs on the dealuminated Beta zeolite support, in which the Cu NPs tend to become smaller under the methanol vapor treatment. This feature enables the realization of an ideal catalyst with superior durability for the hydrogenation of DMO that outperforms the classic Cu-silica–based catalysts. We believe that zeolites with abundant silanol nests act as powerful supports to optimize the dynamic change of Cu NPs, and the reverse ripening concept on this support should open a productive route to more-stable catalysts for industrial processes. By considering the importance of Cu-silica–based catalysts in multiple industrial reaction processes, our work provides a step forward in overcoming the disadvantage of instability and may improve the vitality of scalable applications.

REFERENCES AND NOTES

1. B. C. Gates, *Chem. Rev.* **95**, 511–522 (1995).
2. P. Munnik, P. E. de Jongh, K. P. de Jong, *Chem. Rev.* **115**, 6687–6718 (2015).
3. C. Mondelli, G. Gözaydın, N. Yan, J. Pérez-Ramírez, *Chem. Soc. Rev.* **49**, 3764–3782 (2020).
4. A. T. Bell, *Science* **299**, 1688–1691 (2003).
5. X. Li *et al*., *Nature* **611**, 284–288 (2022).
6. E. V. Makshina *et al*., *Chem. Soc. Rev.* **43**, 7917–7953 (2014).
7. M. B. Gawande *et al*., *Chem. Rev.* **116**, 3722–3811 (2016).
8. S. Hu, W.-X. Li, *Science* **374**, 1360–1365 (2021).
9. J. Jones *et al*., *Science* **353**, 150–154 (2016).
10. J. C. Matsubu *et al*., *Nat. Chem.* **9**, 120–127 (2017).
11. T. W. van Deelen, C. Hernández Mejía, K. P. de Jong, *Nat. Catal.* **2**, 955–970 (2019).
12. Z. Li *et al*., *Nat. Catal.* **1**, 349–355 (2018).
13. M. D. Argyle, C. H. Bartholomew, *Catalysts* **5**, 145–269 (2015).
14. X. Jiang, X. Nie, X. Guo, C. Song, J. G. Chen, *Chem. Rev.* **120**, 7984–8034 (2020).
15. W. Zhou *et al*., *Chem. Soc. Rev.* **48**, 3193–3228 (2019).
16. D. Li *et al*., *Nat. Catal.* **5**, 99–108 (2022).
17. D. R. Palo, R. A. Dagle, J. D. Holladay, *Chem. Rev.* **107**, 3992–4021 (2007).
18. P. Wynblatt, N. A. Gjostein, *Acta Metall.* **24**, 1165–1174 (1976).
19. S. C. Parker, C. T. Campbell, *Phys. Rev. B* **75**, 035430 (2007).
20. R. van den Berg *et al*., *ACS Catal.* **5**, 4439–4448 (2015).
21. D. Yao *et al*., *Nat. Commun.* **14**, 1123 (2023).
22. S. Feng *et al*., *Nat. Commun.* **10**, 5281 (2019).
23. S. Chen *et al*., *Chem. Soc. Rev.* **50**, 3315–3354 (2021).
24. A. Bishara, K. M. Murad, A. Stanislaus, M. Ismial, S. S. Hussian, *Appl. Catal.* **7**, 351–359 (1983).
25. Y. Nishihata *et al*., *Nature* **418**, 164–167 (2002).
26. N. Felvey *et al*., *J. Am. Chem. Soc.* **144**, 13874–13887 (2022).
27. H. Li *et al*., *ACS Catal.* **13**, 1197–1206 (2023).
28. J. Zheng *et al*., *Science* **376**, 288–292 (2022).
29. J. Gong *et al*., *J. Am. Chem. Soc.* **134**, 13922–13925 (2012).
30. J. Lin, X. Zhao, Y. Cui, H. Zhang, D. Liao, *Chem. Commun.* **48**, 1177–1179 (2012).
31. C. Xu *et al*., *Nat. Commun.* **9**, 3367 (2018).
32. J. Sun *et al*., *Sci. Adv.* **4**, eaau3275 (2018).
33. H. Yue *et al*., *AIChE J.* **58**, 2798–2809 (2012).
34. J. Zheng *et al*., *J. Phys. Chem. C Nanomater. Interfaces* **119**, 13758–13766 (2015).
35. C.-S. Chen, W.-H. Cheng, S.-S. Lin, *Chem. Commun.* **2001**, 1770–1771 (2001).
36. Z. Gao, B. Ma, S. Chen, J. Tian, C. Zhao, *Nat. Commun.* **13**, 3343 (2022).
37. C. Wen, Y. Cui, W.-L. Dai, S. Xie, K. Fan, *Chem. Commun.* **49**, 5195–5197 (2013).
38. S. Qing *et al*., *Int. J. Hydrogen Energy* **44**, 16667–16674 (2019).
39. C. D. Chang, A. J. Silvestri, *J. Catal.* **47**, 249–259 (1977).
40. Z. Liu, J. Liang, *Curr. Opin. Solid State Mater. Sci.* **4**, 80–84 (1999).
41. S. Lin *et al*., *J. Am. Chem. Soc.* **143**, 12038–12052 (2021).
42. B. Eren *et al*., *Science* **351**, 475–478 (2016).
43. R.-P. Ye *et al*., *ACS Catal.* **10**, 4465–4490 (2020).
44. K. Ma *et al*., *Chem. Sci.* **10**, 2578–2584 (2019).
45. R. Ouyang, J.-X. Liu, W.-X. Li, *J. Am. Chem. Soc.* **135**, 1760–1771 (2013).
46. Q. Wan *et al*., *Nanoscale* **10**, 17893–17901 (2018).
47. T. W. Hansen, A. T. Delariva, S. R. Challa, A. K. Datye, *Acc. Chem. Res.* **46**, 1720–1730 (2013).
48. Y. X. Zhao, Z. Y. Li, Z. Yuan, X. N. Li, S. G. He, *Angew. Chem. Int. Ed.* **53**, 9482–9486 (2014).
49. Z. Yuan *et al*., *J. Phys. Chem. C Nanomater. Interfaces* **118**, 14967–14976 (2014).

ACKNOWLEDGMENTS

We thank G. Zhu and F. Chen for assistance with TEM characterization and the Center for High Performance Computing at Shanghai Jiao Tong University for providing the computing resources of the Siyuan-1 cluster. We appreciate use of the Hard X-ray Spectroscopy Beamline (BL11B), the User Experiment Assist System, and the Chinese Academy of Sciences–Shanghai Science Research Center of the Shanghai Synchrotron Radiation Facility as well as TILON Group Technology Limited for data collection. We appreciate being able to obtain the SVUV-PIMS measurements through use of the Atomic and Molecular Physics Beamline (BL09U) at the National Synchrotron Radiation Laboratory in Hefei, China. **Funding:** This work was supported by the National Key Research and Development Program of China (2022YFA1503502 and 2019YFA0405602); the National Natural Science Foundation of China (22288101, 22241801, 22202176, 22022302, and 92045303); the China Postdoctoral Science Foundation (2021M702802); the Shanghai Municipal Science and Technology

Major Project (2018SHZDZX03); Group Research Asia of BASF Advanced Chemicals Co., Ltd.; and the Qizhen Project of Zhejiang University. **Author contributions:** L.Liu performed the catalyst preparation, characterization, and catalytic tests. J.L. and X.C. performed the theoretical simulations and wrote the corresponding sections of the paper. Y.Y. and W.R. provided helpful discussions on catalytic performances, catalyst structures, and comparisons with the commercial catalysts. Y.L., X.G., X.T., and L.Li participated in the XRD and XAFS characterizations. H.Li, H.Z., C.W., Q.L., H.W., K.Z., and Y.W. participated in the catalyst synthesis and characterization. M.W., J.M., H.Lou, and Z.W. performed the mass spectra characterization and analyzed the data. L.W. and F.-S.X. designed the study, analyzed the data, and wrote the paper. **Competing interests:** The authors declare no competing interests. **Data and materials availability:** All data are available in the manuscript or the supplementary materials.

SUPPLEMENTARY MATERIALS

science.org/doi/10.1126/science.adj1962
Materials and Methods
Figs. S1 to S62
Tables S1 to S8
References (*50*–*65*)

Submitted 12 June 2023; accepted 5 December 2023
Published online 21 December 2023
10.1126/science.adj1962